



Alkaline Water Electrolysis at 25 A cm^{-2} with a Microfibrinous Flow-through Electrode

Feichen Yang, Myung Jun Kim, Micah Brown, and Benjamin J. Wiley*

The generation of renewable electricity is variable, leading to periodic over-supply. Excess power can be converted to H_2 via water electrolysis, but the conversion cost is currently too high. One way to decrease the cost of electrolysis is to increase the maximum productivity of electrolyzers. This study investigates how nano- and microstructured porous electrodes can improve the productivity of H_2 generation in a zero-gap, flow-through alkaline water electrolyzer. Three nickel electrodes—foam, microfiber felt, and nanowire felt—are studied to examine the tradeoff between surface area and pore structure on the performance of alkaline electrolyzers. Although the nanowire felt with the highest surface area initially provides the highest performance, this performance quickly decreases as gas bubbles are trapped within the electrode. The open structure of the foam facilitates bubble removal, but its small surface area limits its maximum performance. The microfiber felt exhibits the best performance because it balances high surface area with the ability to remove bubbles. The microfiber felt maintains a maximum current density of $25\,000 \text{ mA cm}^{-2}$ over 100 h without degradation, which corresponds to a hydrogen production rate 12.5- and 50-times greater than conventional proton-exchange membrane and alkaline electrolyzers, respectively.

with the addition of 8.5 GW of 4 h electricity storage, modeling showed curtailment remained at 8–10% in the ERCOT system.^[4] Finding additional ways to utilize this excess generation is critical to maximizing the environmental and economic benefits of renewable power as its share of electricity generation increases.

One strategy to utilize excess renewable electricity is to generate H_2 with water electrolysis, an approach that is also referred to as power-to-gas.^[5–14] There are many potential uses of H_2 , including heating, ammonia production, metal refining, conversion into methane or liquid fuels, or use in fuel cell vehicles.^[15] Very large amounts of H_2 can potentially be stored relatively cheaply in underground reservoirs to address the seasonal variability of renewable electricity generation.^[10,16–18] The two most common water electrolysis systems are alkaline and proton exchange membrane (PEM). The alkaline electrolyzer is the

1. Introduction

The variability of electricity generation from wind and solar can lead to mismatches between generation and load which necessitate curtailment of generation. For example, $\approx 4\%$ of electricity generated from wind was curtailed in 2013,^[1] a time at which only 4% of the electricity in the U.S. was generated from wind power.^[2] The curtailment of renewable power by the California independent system operator (CAISO) has increased from 188 GWh in 2015 to 461 GWh in 2018, 95% of which was solar power.^[3] An analysis of the Electricity Reliability Council of Texas (ERCOT) grid system with 55% renewables indicates that at least 11% of the electricity would be curtailed.^[4] Even

most mature technology with a cost roughly half that of PEM electrolyzers.^[5,19] On the other hand, PEM electrolyzers offer higher current densities ($600\text{--}2000 \text{ mA cm}^{-2}$) than alkaline electrolyzers ($200\text{--}450 \text{ mA cm}^{-2}$), enabling them to be more compact.^[19,20]

Without a tax on CO_2 emissions, techno-economic assessments of the feasibility of H_2 production via water electrolysis indicate that it is not cost-competitive with methane steam reforming under current market conditions.^[12,21–23] Thus, commercial applications of electrolyzers are currently limited to small-scale, on-site hydrogen production for industrial applications, with a few larger-scale plants for ammonia fertilizer production in remote areas with excess electricity.^[19] The opportunity to utilize low-cost, excess electricity from renewable generation will help to make water electrolysis cost competitive, but reductions in the cost of the electrolyzer plant will also be necessary.^[24,25] One way to lower the electrolyzer cost and take advantage of periodically low electricity prices is to increase the amount of H_2 such plants can produce, i.e., their productivity, without degrading their lifetime.^[19]

The formation of gas bubbles currently limits the maximum current density, and thus productivity, of alkaline electrolyzers.^[19,26] A variety of attempts have been made to address the bubble removal problem, including circulation of electrolytes across the surface of the electrode,^[19,26–28] development of zero gap and other advanced electrolyzer architectures,^[29–33]

F. Yang, Prof. M. J. Kim, Dr. M. Brown, Prof. B. J. Wiley
Department of Chemistry
Duke University
124 Science Drive, Box 90354, Durham, NC 27708, USA
E-mail: benjamin.wiley@duke.edu

Prof. M. J. Kim
Department of Applied Chemistry
Kyung Hee University
Yongin 17104, Republic of Korea

The ORCID identification number(s) for the author(s) of this article can be found under <https://doi.org/10.1002/aenm.202001174>.

DOI: 10.1002/aenm.202001174

application of magnetic fields,^[34–36] application of ultrasonic fields,^[37] and even modifications to the gravitational field.^[28,38,39] Approaching this problem from the perspective of material scientists, we are particularly interested in how the structure of the electrode can be modified to improve bubble removal while retaining a large surface area for water electrolysis.

There are a huge number of studies of how electrode structure affects the efficiency of water electrolysis, but relatively few studies have focused on the effect of electrode structure on bubble removal and the maximum current density.^[40–43] For example, a study of electrodeposited Ni catalysts with different morphologies indicated a needle-like morphology exhibited a high current density due to its low surface tension which facilitated bubble removal. Studies of 3D porous electrodes have attributed their high performance to their ability to remove bubbles.^[40,42,44] However, it is not yet clear what is the optimum electrode structure that will maximize surface area for electrolysis without hindering bubble removal. It is also not clear what is the maximum current density for different 3D porous electrode structures.

This study sought to address the question of what is the ideal electrode structure that maximizes the surface area for water electrolysis while facilitating bubble removal at high current densities. A zero-gap, flow-through electrode geometry was adopted to minimize the distance between the electrodes and maximize the ability of flowing fluid to remove bubbles from the porous electrode surface. Three Ni porous electrodes—foam, microfiber (MF) felt, and nanowire (NW) felt—were tested to examine the tradeoff between pore diameter and surface area. Although the NW felt had a surface area 1.34 times larger than the MF felt, it exhibited an overpotential 41 mV higher than the MF felt at a current density of 100 mA cm⁻². Pulse electrolysis

revealed the overpotential for the NW felt was initially lower than the MF felt, but quickly rose to exceed that of the MF felt within 1 min. The corresponding decrease in the permeability of the electrode over the same period suggested that bubble entrapment limited the performance of the NW felt. The greater entrapment of bubbles within the NW felt was ascribed to the greater pore-throat aspect ratio and the smaller size of the pore throat relative to the gas bubbles. The MF felt also exhibited better performance than the Ni foam due to its higher surface area. The MF felt thus represents an optimal trade-off between surface area and pore throat geometry for bubble removal. MF felts exhibited H₂ production rates 1.7 and 6.7 times greater at an energy efficiency of 50% (based on the lower heating value of H₂) compared to conventional PEM and alkaline water electrolyzers, respectively. The maximum current density of the MF felt was 25 000 mA cm⁻² at 3.6 V which is 12.5 and 50 times greater than the current density from PEM and alkaline water electrolyzers, respectively. The greater production rate enabled by MF felts can improve the economics for conversion of inexpensive, excess renewable energy to H₂.

2. Results and Discussion

2.1. Physical Properties of Ni Foam, Ni Microfiber Felt, and Ni–Cu Nanowire Felt

To investigate how pore size and surface area affect the performance of alkaline water electrolysis, three electrodes, Ni foam, Ni MF felt, and Ni–Cu NW felt, were studied with a flow cell shown in **Figure 1a** (also see Figure S1, Supporting Information). We used Cu NWs as a core for Ni-covered NWs because

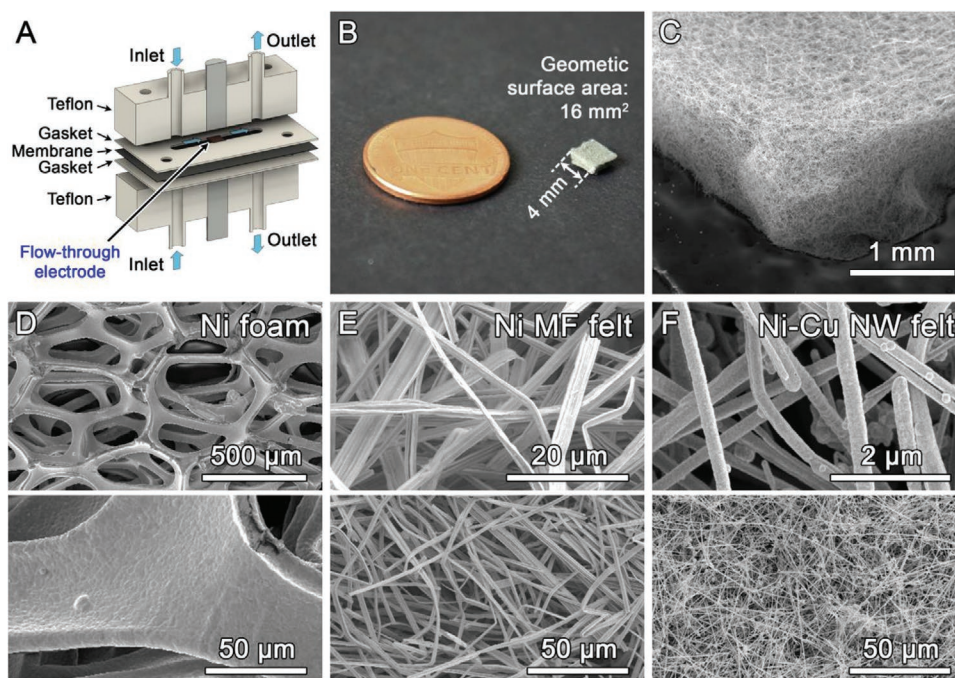


Figure 1. a) A diagram of the flow cell used in this study. b) Photo and c) low-magnification SEM image of Ni MF felt. High-magnification SEM images of d) Ni foam, e) Ni MF felt, and f) Ni–Cu NW felt. The bottom images in (d–f) have the same magnification.

we previously developed a large-scale synthesis of Cu NWs.^[45,46] This large-scale synthesis facilitates electrode fabrication. In addition, there are no syntheses of Ni nanowires with a stick-like morphology and dimensions appropriate for the fabrication of a highly porous flow-through electrode.^[47] Figure S2 (Supporting Information), an energy dispersive X-ray spectroscopy image, shows the uniform Ni shell around the Cu nanowire. An X-ray photoelectron spectroscopy (XPS) spectrum in Figure S3 (Supporting Information) indicates that Cu was not exposed after Ni coating, so that Cu did not affect the water-splitting performance of the Ni–Cu NW felts. Ni MFs were coated by Ni to exclude the effect of impurities in as-received Ni MFs. The Ni MF and Ni–Cu NW felts were prepared via filtration and then annealed to maximize their electrical conductivity (Figure 1b,c; and Figure S4, Supporting Information).^[48] Before annealing, it was not possible to use the MF and NW felts for flow electrolysis due to their low mechanical strength and low electrical conductivity. The XPS results for the electrodes confirmed that the electronic structure of Ni in the three electrodes was the same (Figure S5, Supporting Information), indicating they should have the same electrocatalytic activity, and that the differences in the electrochemical performance of the three electrodes are due to their different microstructures.

Figure 1d–f shows the morphology of Ni foam, Ni MF felt, and Ni–Cu NW felt. Low-magnification scanning electron microscopy (SEM) images for Ni foam and Ni–Cu NW felt are shown in Figure S6 (Supporting Information). The physical properties of the electrodes are listed in Table 1. All three electrodes were electrically conductive and highly porous (porosity: 0.93–0.96). The pore and pore-throat diameters (illustrated in Figure S7, Supporting Information) and specific surface area of each material were significantly different. The average pore-throat diameter for the Ni–Cu NW felt, Ni MF felt, and Ni foam measured from SEM images was 3.3, 19, and 226 μm , respectively, spanning three orders of magnitude. The Ni–Cu NW felt had the greatest specific surface area, followed by the Ni MF felt and Ni foam (Table 1; and Figure S8, Supporting Information). Since larger pores with a smaller surface area facilitate liquid flow at a given pressure as described in Darcy's law and the Kozeny–Carman equation,^[49,50] the Ni foam had the greatest permeability, followed by the Ni MF and Ni–Cu NW felts (Table 1; and Figure S9, Supporting Information). Although the permeability of the Ni–Cu NW felt was on the order of 10^{-13} m^2 , the pressure required for liquid flow at 2 mL min^{-1} was only

3.59 atm (through the 0.02 cm^2 cross-sectional area of the $500 \mu\text{m}$ thick, 0.4 cm wide electrode used in this study), which is similar to the water pressure in a house ($\approx 3\text{--}4 \text{ atm}$).

2.2. Effect of Surface Area and Pore Structure on Water Electrolysis

We now discuss how the pore dimensions and surface area of the electrodes affect their productivity. If gas bubbles can travel easily through a porous electrode, increasing the specific surface area will increase the productivity. In such a case, the Butler–Volmer formula predicts the Ni–Cu NW felt would have the greatest productivity. On the other hand, if gas bubbles are trapped within the porous electrode, they will block the surface and reduce the productivity of the electrode. Thus, the optimal electrode structure should be one that maximizes the active surface area while still allowing for rapid removal of gas bubbles.

To determine the conditions under which surface area or bubble removal limits the productivity of the electrodes, linear sweep voltammetry for the oxygen evolution reaction (OER) was performed in 1 M KOH aqueous solution (Figure 2a). The current density (normalized by the geometric surface area of the electrode, 16 mm^2 , Figure 1b) of the Ni MF felt was the greatest, followed by Ni–Cu NW felt and Ni foam. To achieve a current density of 100 mA cm^{-2} , the Ni MF felts required a 349 mV overpotential, versus 390 mV for Ni–Cu NW felt and 473 mV for Ni foam (see also Table S1, Supporting Information). In the magnified voltammograms (Figure S10, Supporting Information), the onset potentials were between 1.52 and 1.55 V, similar to the range of onset potentials reported for Ni electrodes in the literature ($1.53\text{--}1.55 \text{ V}$).^[51,52] Such a small difference in onset potential (0.03 V) indicates the intrinsic activities of Ni in the three electrodes are comparable, and cannot account for the large difference in the observed current densities. Thus, the differences in the currents in Figure 2a were caused by the different pore size and surface area of each electrode.

To understand why the Ni MF felt exhibited the highest OER performance, we considered two factors: i) the current density normalized by the electrochemically active surface area (ECSA) and ii) the ability of the three electrodes to remove gas. Note that the current density normalized by the ECSA (j_{ECSA}) was only used for Figure 2b, and the rest of the current densities were

Table 1. Physical properties of Ni Foam, Ni MF felt, and Ni–Cu NW felt.

	Ni foam	Ni MF felt	Ni–Cu NW felt
Fiber diameter [μm]	—	1.70	0.35
Electrical resistivity [$\text{m}\Omega \text{ cm}$]	0.08	1.88	0.67
Porosity	0.94	0.93 ^{a)}	0.96 ^{a)}
Permeability [m^2]	Too high to measure	1.76×10^{-12}	2.30×10^{-13}
Pore diameter [μm]	400 ^{b)}	46.9 ^{c)}	17.1 ^{c)}
Pore-throat diameter [μm] ^{d)}	226 ± 33	19 ± 6.2	3.3 ± 1.1
Specific surface area [$\text{m}^2 \text{ m}^{-3}$]	4.80×10^3	4.40×10^5	5.90×10^5

^{a)}After compression from a thickness of 800 to 500 μm ; ^{b)}Average pore size provided by the vendor; ^{c)}Calculated using Equation (2); ^{d)}Measured from SEM images.

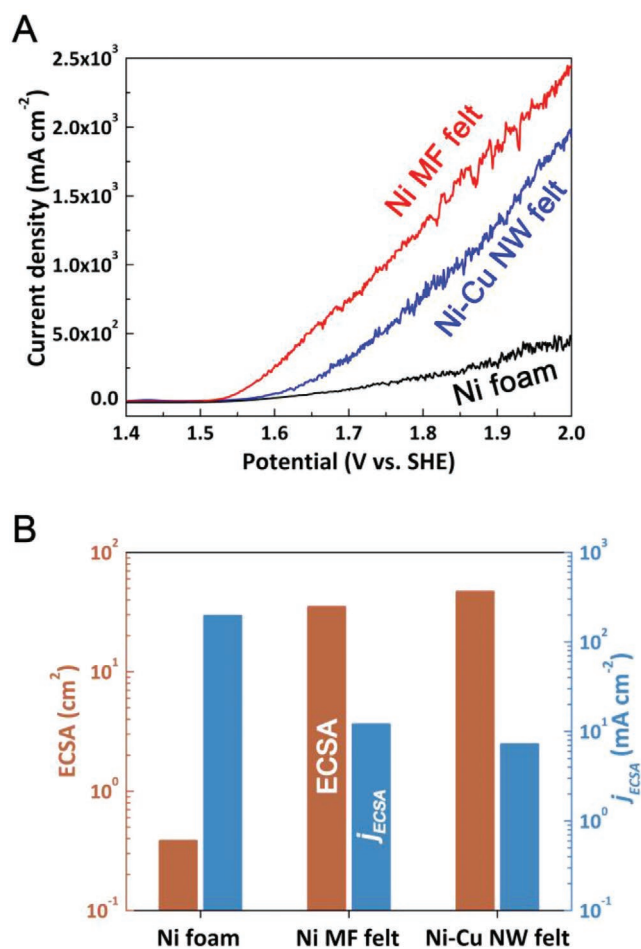


Figure 2. a) Linear sweep voltammograms for the OER with Ni foam, Ni MF felt, and Ni-Cu NW felt. b) ECSA for a given volume ($4 \times 4 \times 0.5 \text{ mm}^3$) and j_{ECSA} at a potential (vs SHE) of 1.980 V (i.e., an overpotential of 0.750 V) for the Ni foam, Ni MF felt, and Ni-Cu NW felt.

normalized by the geometric area of the electrodes (16 mm^2). The ECSA of each electrode was determined using the capacitive current density (Figure S8, Supporting Information).

Figure 2b shows the ECSA for the volume ($4 \times 4 \times 0.5 \text{ mm}^3$) of the electrode and the j_{ECSA} for the three electrodes at an overpotential of 0.75 V (i.e., 1.980 V vs the standard hydrogen electrode (SHE)). The ECSA of the Ni-Cu NW felt was the highest, followed by Ni MF felt and Ni foam. In contrast, the j_{ECSA} exhibited the opposite trend: Ni-Cu NW felt < Ni MF felt < Ni foam. If the OER follows the Butler-Volmer formula,^[53] the j_{ECSA} of the three electrodes should be similar. Also, assuming the electrocatalytic activity of each electrode material is the same, the Tafel slope (i.e., $(1-\alpha)F/2.3RT$ where α , F , R , and T are the transfer coefficient, Faraday constant, gas constant, and temperature, respectively)^[53] should be identical as well. However, as shown in Figure S11 (Supporting Information), the three electrodes exhibited different Tafel slopes. The Ni MF felt had the lowest Tafel slope (88.8 mV dec^{-1}), followed by the Ni-Cu NW felt (97.3 mV dec^{-1}) and Ni foam ($104.6 \text{ mV dec}^{-1}$). Given all three electrodes are Ni and exhibit the same onset potential, the differences in the Tafel slope

and j_{ECSA} for the three electrodes should be due to their different ability to remove bubbles.

We performed pulse electrolysis to clarify the effect of bubble removal on the performance of these porous electrodes. During pulse electrolysis, a constant current of 500 mA cm^{-2} was applied during the On-period, followed by a period of no current during a 5 min long Off-period. The electrolyte flow rate was fixed at 1 mL min^{-1} , corresponding to a superficial velocity of 0.833 cm s^{-1} . The Off-period provides time for bubble removal and recovery of any surface area that was blocked by the bubbles. However, if the bubbles are confined and cannot be removed, the cell potential will increase after each On-period due to blockage of the electrode surface by bubbles and the loss of active surface area. The pressure drop across the electrode will also increase if bubbles are confined within the electrode because they will reduce the number of paths for liquid flow.

Figure 3a depicts the change in the cell potential and pressure drop for the Ni MF and Ni-Cu NW felts during pulse electrolysis. The pressure drop (P) during electrolysis was normalized by the initial pressure drop (P_0) obtained when electrolyte flowed through the porous electrodes without an applied voltage. Both electrodes exhibited an increase in the cell potential and P/P_0 during the On-period. During the Off-period, the P/P_0 for both electrodes decreased due to the removal of the gas bubbles. We confirmed the electrode reached a steady-state in each Off-period from the plateau in P/P_0 . However, the cell potential and P/P_0 increased to a much greater extent for the Ni-Cu NW felt compared to the Ni MF felt. During the first cycle of pulse electrolysis, the Ni-Cu NW felt exhibited an increase in the cell potential of 0.44 V, and an increase in P/P_0 of 2.8 times. In comparison, for the Ni MF felt the cell potential increased by 0.14 V and P/P_0 increased 1.9-fold. In addition, the starting cell potential for each On-period increased for the Ni-Cu NW felt. By the third cycle, the Ni-Cu NW felt required a 270 mV greater potential than the first cycle to drive the same current. In contrast, the cell potential at the start of each On-period for the Ni MF felt did not change.

The change in the cell potential for the Ni foam during pulse electrolysis was also monitored, but the pressure change during pulse electrolysis with the Ni foam could not be measured due to the high permeability of Ni foam. Figure S12 (Supporting Information) indicates that bubbles increased the cell potential for the Ni foam to a lesser extent than the other electrodes. In the first cycle of pulse electrolysis, the increase in the cell potential with the Ni foam was 0.12 V, while those for Ni-Cu NW and Ni MF felts were 0.44 and 0.14 V (Figure 3a).

The cell potential of the Ni-Cu NW felt during the first and the second cycles was initially lower than that of the Ni MF felt, but the Ni-Cu NW felt lost this performance advantage once bubbles were trapped within the pores of the electrode. In addition to retaining its initial potential, the P/P_0 for the Ni MF felt increased only 10% after three cycles of pulse electrolysis. In comparison, the P/P_0 for the Ni-Cu NW felt increased by 55%, providing further evidence that the NW electrode performance was limited by bubble entrapment. The results of pulse electrolysis show that the effect of the gas bubbles on the performance of water splitting was the smallest for the Ni foam, followed by the Ni MF felt and the Ni-Cu NW felt.

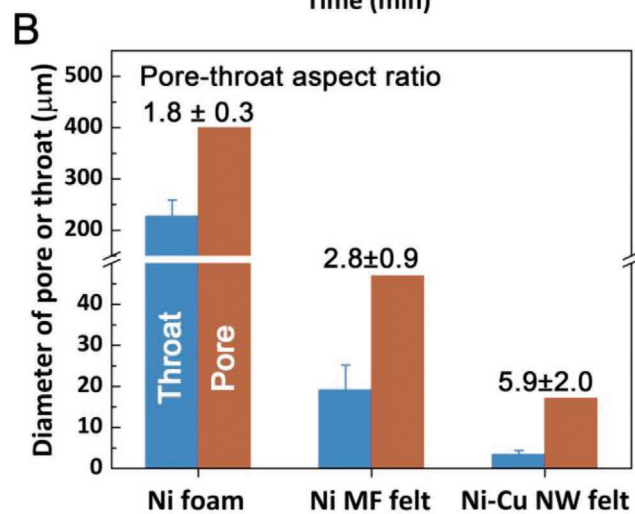
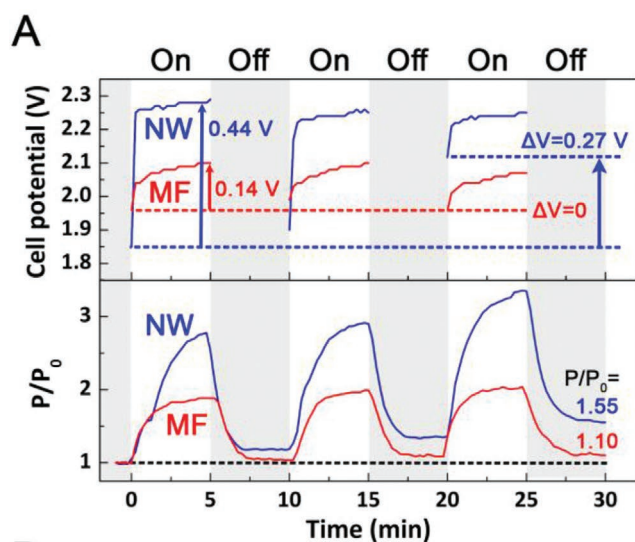


Figure 3. a) Changes in the cell potential and pressure drop (P/P_0) during pulse electrolysis with Ni MF and Ni-Cu NW felts. A current density of 500 mA cm^{-2} was applied for 5 min (On-period), after which electrolysis was stopped for 5 min (Off-period, shaded region). The electrolyte was a 1 M KOH aqueous solution with a superficial velocity of 0.833 cm s^{-1} . b) The average pore diameter, throat diameter, and pore-throat aspect ratio for the Ni foam, Ni MF felt, and Ni-Cu NW felt.

The mechanism for the displacement of gas bubbles by the electrolyte in the porous electrode must be considered to understand how the electrode structure affects bubble entrapment. The situation can be considered as two-phase flow in porous media consisting of a wetting (electrolyte) and nonwetting (gas bubbles) phases.^[54–58] Two primary mechanisms govern bubble removal: snap-off and frontal displacement. Frontal displacement refers to gas bubbles getting pushed through the porous media by the electrolyte like a piston, resulting in removal of the gas bubbles. Snap-off refers to the electrolyte wetting the surface of the pores (which are initially filled with gas), and forming a meniscus at the pore throat. Snap-off results in gas bubbles being surrounded by the electrolyte and confined in the pores.

The amount of frontal displacement versus snap-off is affected by the capillary number and the pore-throat aspect

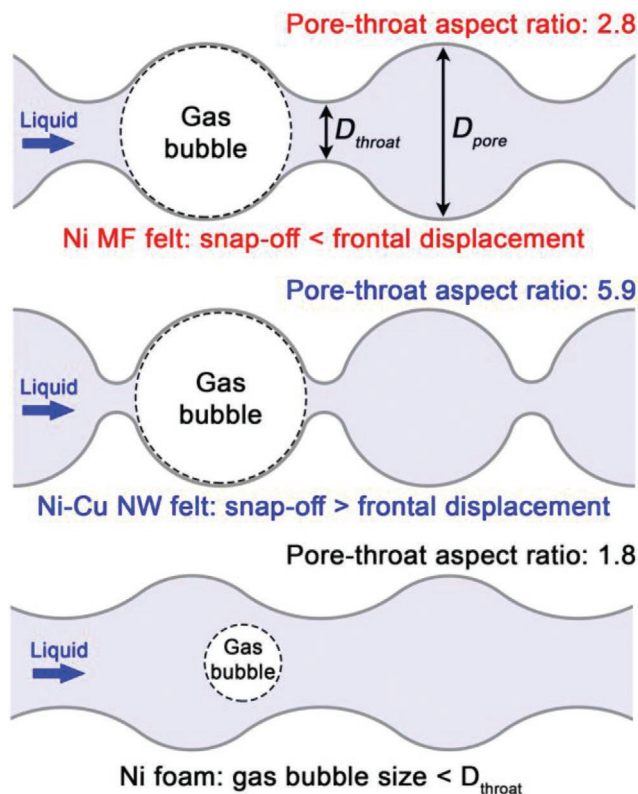


Figure 4. Diagram of gas bubbles traveling through the pores with pore-throat aspect ratios of 2.8 (Ni MF felt), 5.9 (Ni-Cu NW felt), and 1.8 (Ni foam).

ratio. As the capillary number ($Ca = \mu u / \sigma$) is a function of the viscosity of the fluid (μ), the superficial velocity (u), and the interfacial tension (σ), it should be similar for all of the electrodes, and thus cannot explain the difference in electrode performance. Thus, the pore-throat aspect ratio (the diameter ratio of pore to throat) is likely to govern the amount of bubble entrapment.^[54–58] The effect of the pore-throat aspect ratio on bubble entrapment is illustrated in **Figure 4**. Basically, if the throats between the pores are much smaller than the pores, bubbles that grow to the size of the pores will be trapped within them. The effect of the pore-throat aspect ratio on frontal displacement versus snap-off can be described quantitatively with the following equation^[54]

$$\frac{P_{\text{snap-off}}}{P_{\text{frontal displacement}}} = \frac{1}{C_{I_n}} \left(\frac{D_{\text{pore}}}{D_{\text{throat}}} \right) (1 - \tan \theta \cdot \tan \alpha) \quad (1)$$

where P is the threshold capillary pressure for snap-off or frontal displacement, C_{I_n} is a constant related to the number of throats per pore (n), D is the diameter, θ is the contact angle, and α is the half-angle of the corners ($\alpha = [90(n-2)/n]$).^[59] As the pores in each electrode have multiple pore throats, the value of C_{I_n} can be taken as 0.5 ($n \geq 4$).^[54] Therefore, the snap-off versus frontal displacement is determined by the ratio of the pore diameter to pore-throat ($D_{\text{pore}}/D_{\text{throat}}$), α , and θ .

The average D_{throat} of the electrodes was measured from SEM images (Figure 1d–f). The D_{pore} of the electrodes was calculated from the following equation^[60]

$$D_{\text{pore}} \equiv \frac{2w}{\ln(1/\varepsilon)} \quad (2)$$

where w is the diameter of the constituent fibers and ε is the porosity. The values of D_{pore} , D_{throat} , and $D_{\text{pore}}/D_{\text{throat}}$ for the three electrodes are summarized in Figure 3b and Table 1. The $D_{\text{pore}}/D_{\text{throat}}$ for the three electrodes was 5.9 ± 2.0 for Ni–Cu NW felt, 2.8 ± 0.9 for Ni MF felt, and 1.8 ± 0.3 for the Ni foam.

As described in a previous report,^[54] the large $D_{\text{pore}}/D_{\text{throat}}$ value for the Ni–Cu NW felt is more likely to induce snap-off of the gas bubbles, leading to their entrapment and a lower permeability to fluid flow. The smaller pore-throat aspect ratios of the Ni MF felt and Ni foam indicate that snap-off is less likely to occur for these electrodes. Our findings are supported by previous research suggesting that a decrease in the $D_{\text{pore}}/D_{\text{throat}}$ from 6.8 to 1.7 could increase the contribution of frontal displacement to the pore-filling process, resulting in lower residual saturation of gas bubbles.^[54] As a result of the different $D_{\text{pore}}/D_{\text{throat}}$ for the electrodes, the entrapment of gas bubbles goes as Ni foam < Ni MF felt < Ni–Cu NW felt.

Next, we consider the role of α , the half-angle of the corners. As stated above, $\alpha = [90(n-2)/n]$ where n is the number of throats per pore. Therefore, $\tan \alpha$ increases with n , meaning that more throats per pore makes the snap-off process more favorable. The number of throats per pore can be approximately determined by dividing the surface area of a pore (πD_{pore}^2) by the area of a throat ($\pi D_{\text{throat}}^2/4$), assuming that the pore and the throat are a sphere and circle, respectively, $n \approx 4(D_{\text{pore}}/D_{\text{throat}})^2$. The equation, $4(D_{\text{pore}}/D_{\text{throat}})^2$, gives n values of 139 for the NW felt and 31 for the MF felt, corresponding to the values of α of 88.7° and 84.2° . Thus $\tan(\alpha_{\text{NW}}) \approx 44.1$, while $\tan(\alpha_{\text{MF}}) \approx 9.5$. The higher value of the tangent of α_{NW} for NW felt again implies that snap-off is more favored within the NW felt due to the greater $D_{\text{pore}}/D_{\text{throat}}$.

The influence of contact angle (θ) is more complicated because the contact angle continuously changes with the movement of bubbles.^[61] Although the apparent contact angles for the three electrodes are similar (Figure S13, Supporting Information), the dynamic contact angle in each electrode depends on the values of $D_{\text{pore}}/D_{\text{throat}}$. To compare the effect of contact angle for the MF and NW felts, we consider the contact angles when a pore is completely filled with a gas bubble, i.e., $D_{\text{bubble}} \approx D_{\text{pore}}$. The contact angle can be calculated from $\cos \theta = D_{\text{throat}}/D_{\text{bubble}} \approx D_{\text{throat}}/D_{\text{pore}}$.^[62] This equation gives the θ values of 69° for MF felt and 80° for NW felt. As $\tan \theta = 5.7$ for the NW felt and $\tan \theta = 2.6$ for the MF felt, these results again indicate the snap-off process is more favorable for the NW felt than the MF felt.

Of course, regardless of the value of $D_{\text{pore}}/D_{\text{throat}}$, α , and θ , if the bubbles are much smaller than D_{throat} , they can be easily displaced from the electrode. Thus, it is also necessary to consider the size of the gas bubbles relative to D_{throat} . Since it is difficult to directly measure the average bubble size within each electrode, we determined the maximum size of gas bubbles when only a buoyant force exists with a Ni mesh electrode. A

dark-field microscope image in Figure S14 (Supporting Information) shows the average bubble size at departure was $33 \mu\text{m}$ (± 15). We note that the bubble diameter for a Ni mesh electrode in a solution of 31 wt% KOH at 80°C was previously measured to be $\approx 100 \mu\text{m}$ with a camera equipped with a macro lens.^[63] For either bubble size, the size of the bubbles was smaller than the D_{throat} and D_{pore} for the Ni foam but larger than the D_{throat} for the Ni MF and Ni–Cu NW felts. Therefore, bubbles can easily escape from the Ni foam since their maximum size is less than the D_{throat} of the Ni foam (Figure 4, bottom). However, it is possible the gas bubbles can be larger than the D_{throat} of the Ni MF and Ni–Cu NW felts, increasing the resistance to bubble removal (Figure 4). As predicted by both the bubble size versus D_{throat} and $D_{\text{pore}}/D_{\text{throat}}$ value, resistance to bubble removal takes the following order: Ni foam (Figure 4, bottom) < Ni MF felt (top) < Ni–Cu NW felt (middle).

In summary, the OER current densities shown in Figure 2a (Ni MF felt > Ni–Cu NW felt > Ni foam) can be understood by the ECSA of the electrodes and gas entrapment. The Ni MF felt exhibited the best performance because it has a greater surface area while maintaining an adequate ability to remove gas bubbles. Although the specific surface area of the Ni–Cu NW felt was 1.34 times greater than the Ni MF felt, the smaller D_{throat} and $D_{\text{pore}}/D_{\text{throat}}$ values lead to greater entrapment of bubbles within the electrode, and thus a decrease in the active surface area of the electrode. The fact that D_{throat} is larger than the diameter of the bubbles for the Ni foam facilitated bubble removal, but Ni foam exhibited the lowest OER performance because the ECSA of the Ni foam was 92 times smaller than the Ni MF felt. Additional simulations^[64,65] and experimental observations^[66,67] for bubble transport within NW and MF felts could provide more detailed analytical results that enable a quantitative connection between bubble transport phenomena and OER performance.

2.3. Maximum Productivity of Alkaline Water Electrolysis with Ni Microfiber Felts

The Ni MF felt proved to be the best porous electrode for water electrolysis because it provided an optimal balance between surface area and bubble permeability. We conducted further experiments with different flow rates and cell potentials to determine what was the maximum productivity (i.e., the maximum current density for water electrolysis) for the Ni MF felt in a flow-through reactor. Figure 5a,b shows that the relationship between the current density, cell potential, and flow rate depended on the cell potential. Between 2 and 2.5 V (Figure 5a), the current density increased with increasing flow rate, presumably due to the liquid flow facilitating bubble removal. However, above 3 V, the current density decreased with increasing flow rate (Figure 5b). We hypothesize this is due to resistive heating of the electrolyte, which will cause a greater temperature increase at lower flow rates. Higher temperatures will in turn reduce the charge transfer resistance for OER as described in the Butler–Volmer equation.^[53] However, excessive resistive heating burned the membrane and caused that the anode and cathode to short-circuit (the green-shaded region in Figure 5b). The burned and melted membrane after

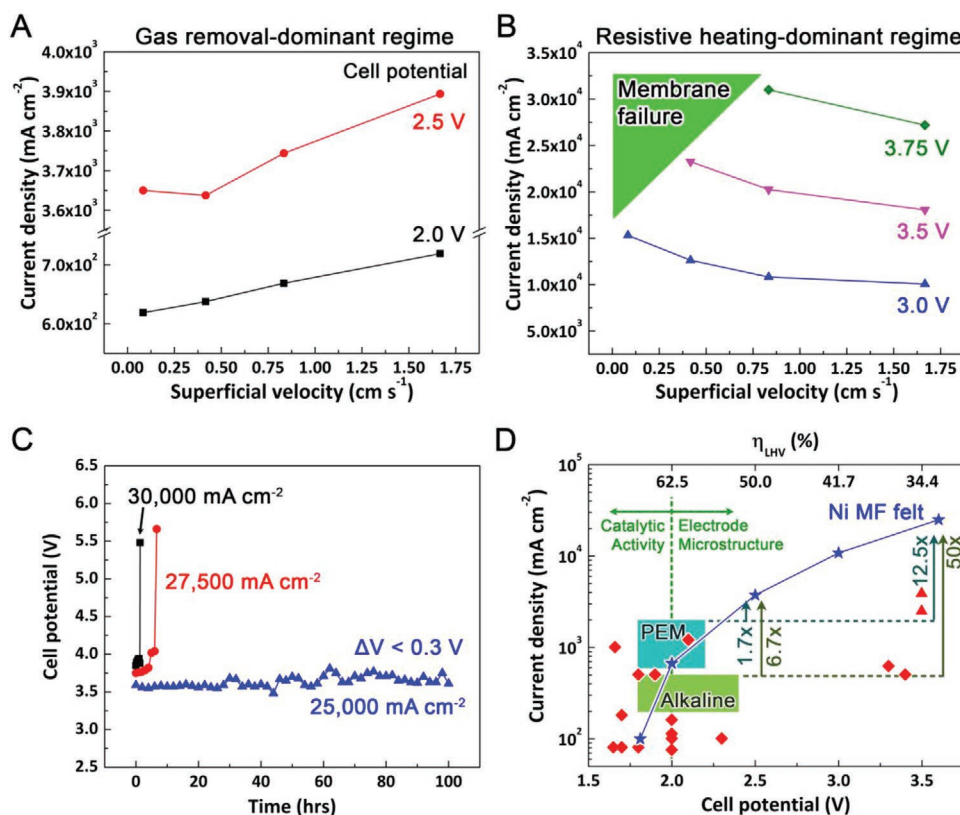


Figure 5. Water electrolysis with the Ni MF felt in two regimes: a) gas removal-dominant (cell potential: 2–2.5 V) and b) resistive heating-dominant (cell potential: 3–3.75 V). c) The cell potential versus time for constant current densities of 25 000, 27 500, and 30 000 mA cm⁻². d) The water electrolysis performance of the Ni MF felt as a function of the cell potential. The current densities were measured in a 30 wt% KOH aqueous solution at a superficial velocity of 0.833 cm s⁻¹. The boxes shaded in green and aquamarine correspond to the operating cell potentials and current densities for industrial alkaline and PEM electrolyzers, respectively.^[19,20] Red symbols correspond to maximum current densities for alkaline electrolysis reported in the literature.^[32,52,70–87] The red triangles at 3.5 V are for membraneless flow-through alkaline electrolyzers.^[32,87]

electrolysis is shown in Figure S15 (Supporting Information). The maximum current density without membrane degradation for 5 min was 31 000 mA cm⁻² at 3.75 V with a superficial velocity of 0.833 cm s⁻¹.

Since it is important that operation of an electrolyzer at high current densities does not reduce its lifetime, we further investigated the long-term stability of the Ni MF felt by applying a constant current density of 30 000 mA cm⁻² (Figure 5c). At this current, the cell potential spiked after 1.2 h due to continuous degradation of the membrane by resistive heating. The current density of 27 500 mA cm⁻² also resulted in cell failure after 6 h. By reducing the applied current density to 25 000 mA cm⁻², the driving voltage remained stable for 100 h (Figure 5c). At this current density, the Faradaic efficiency was 98–99% (Figure S16, Supporting Information), as determined by the volume of the produced gas. The electrode experienced a weight fluctuation of 0.2 mg over this period, which was within the error of the measurement (Figure S17, Supporting Information). This weight fluctuation of 0.2 mg corresponds to 4.6×10^{-5} % of the total current that was used in the long-term test (25 000 mA cm⁻², 100 h), indicating that the electrode was not undergoing corrosion ($\text{Ni}^0 \rightarrow \text{Ni}^{2+} + 2\text{e}^-$) during this period. As indicated in the Pourbaix diagram for Ni,^[68] the electrode surface likely consists of gamma phase Ni(OH)₂, which imparted

corrosion resistance.^[69] XPS results indicate the electronic structure of Ni in Ni(OH)₂ remained the same for 100 h (Figure S18, Supporting Information), and no apparent degradation of MFs was observed in SEM images (Figure S19, Supporting Information). In addition, the membrane was visually examined every 12 h and no degradation was apparent at a current density of 25 000 mA cm⁻². We note there was a fluctuation in the cell potential (<0.3 V) over this period. This fluctuation was most likely caused by a change in the contact resistance to the electrode after the repeated disassembly and assembly of the flow cell to measure the change in the weight of the MF felt. Based on the results of the long-term stability test, the maximum current density for alkaline water electrolysis with the Ni MF felt was determined to be 25 000 mA cm⁻² at a cell potential of 3.6 V.

Figure 5d compares the alkaline water electrolysis performance of the Ni MF felt to industrial PEM and alkaline water electrolyzers. The current density for the Ni MF felt was comparable to industrial alkaline electrolyzers at cell potentials lower than 2 V. At cell potentials greater than 2 V, the Ni MF felt achieved a current density comparable to conventional PEM electrolyzers, and surpassed the maximum performance of PEM electrolyzers at cell potentials greater than 2.31 V. The energy efficiency, $\eta_{\text{LHV}} (\%) = 1.25/\text{cell potential (V)} \times 100$, based

on the lower heating value (LHV) of H₂ for conventional water electrolysis, is generally recommended to exceed 50%,^[19,20,88] corresponding to a cell potential of 2.5 V (Figure 5d). At this boundary, the Ni MF felt a current density 1.7 and 6.7 times greater than conventional PEM and alkaline electrolyzers, respectively. The lower current densities of alkaline water electrolyzers has been considered their main drawback compared to PEM electrolyzers.^[20,88,89] The higher current density achieved with the Ni MF suggests it can achieve a better balance of surface area and bubble removal ability compared to the electrode structures (e.g., perforated plates or mesh) currently used in commercial alkaline water electrolyzers,^[90] and allow them to achieve higher current densities than PEM electrolyzers.

Even higher current densities are relevant in situations when electricity costs are zero or negative due to a periodic oversupply of electricity. Under such conditions, one would want to operate the electrolyzer at its maximum rated current density without regard for energy efficiency. The maximum current density for the Ni MF felt was 50- and 12.5-fold greater than conventional alkaline and PEM water electrolyzers,^[19,20] respectively. This result suggests that alkaline electrolysis with the Ni MF felt would greatly improve the costs for conversion of electricity into H₂ when electricity costs are zero or negative.

We further compared the performance of Ni MF felts with the maximum current densities for alkaline electrolysis reported in the literature (red symbols in Figure 5d; and Table S2, Supporting Information). This comparison indicates that the electrocatalytic activity of the electrode material dominates the electrolysis performance at cell potentials below 2.0 V. Although the maximum current density for Ni MF felt (670 mA cm⁻² at 2.0 V) was higher than most other electrocatalysts, a higher performance can be achieved by improving the electrocatalytic activity of the electrode material.

On the other hand, the modification of electrode microstructure and cell configuration is more critical when the cell potential exceeds 2.0 V. In this potential regime, it is difficult to exceed a current density of 1000 mA cm⁻² by only changing the electrocatalytic activity. For example, Co₂P and IrO₂/Pt electrodes could achieve only 500 mA cm⁻² at cell potentials of 3.36 and 4.31 V, respectively.^[86] Only membraneless flow-through electrodes (red triangles in Figure 5d) achieved a much higher current density of 3900 mA cm⁻² at 3.5 V.^[32,87] Furthermore, superaerophobic Ni phosphide nanoarrays achieved a current density of 1200 mA cm⁻² at the cell potential of 2.1 V by enhancing the bubble departure from the electrode surface. These results indicate that promoting the departure of gas bubbles from the electrode surface is essential to break through the current density of 1000 mA cm⁻². This study shows the use of a Ni MF felt in a flow-through configuration essentially eliminates bubble removal as a factor that limits the maximum current density, and thereby enables a 6.4-fold increase in the maximum current density over what had been achieved with a membraneless flow-through alkaline electrolyzer in previous research (3900 mA cm⁻² at 3.5 V).^[32] At current densities in excess of 25 000 mA cm⁻², resistive heating and associated degradation of the polyethersulfone membrane limit the maximum current density that can be achieved. Higher current densities may be possible by using a membrane that remains stable at high temperatures.

3. Conclusion

This study explored how the structure of an electrode impacts the maximum productivity for alkaline electrolysis in a zero-gap, flow-through reactor. Linear sweep voltammetry showed that Ni microfiber felt exhibited a lower overpotential (330 mV at 100 mA cm⁻²) than Ni-Cu nanowire felt (390 mV), even though its surface area was 25% smaller. Pulse electrolysis experiments showed the nanowire felt initially had a lower overpotential than the microfiber felt, but the overpotential rose to be larger than that of the microfiber felt in less than 1 min due to greater entrapment of bubbles in the nanowire felt. The greater degree of bubble entrapment in the nanowire felt was caused by the greater pore-throat aspect ratio, and the greater ratio of the bubble diameter to the pore throat. Ni foam did not trap bubbles because of its large pore throats, but Ni foam had a higher overpotential (470 mV at 100 mA cm⁻²) because of its relatively low surface area. The microfiber felt thus represents an optimal trade-off between surface area and bubble removal for water electrolysis. A flow-through alkaline electrolyzer with microfiber felt electrodes maintained a current density of 25 A cm⁻² over 100 h. This current density is 12.5- and 50-times greater than conventional alkaline and PEM electrolyzers, respectively, and is 6.4 times higher than the next highest current density reported in the literature. The use of microfiber felts for water electrolysis can therefore lower the cost of H₂ produced by alkaline electrolysis by increasing the productivity of electrolyzers, and by taking better advantage of low electricity costs due to oversupply from renewable energy sources.

We expect that further improvements in the electrode design may lead to even greater performance. For example, one might introduce shallow, nanoscale pores or needles on the surface of the microfibrils to further increase surface area without hindering bubble removal. Also, more advanced methods to accurately control the structure and dimensions of pores in flow-through electrodes could minimize bubble entrapment while maximizing the surface area for water splitting. Development of improved electrode structures would be facilitated by additional visualization and modeling of bubble transport through such electrodes.^[63,67] Alternatively, one could coat the microfibrils with a better catalyst than Ni to further boost the performance. The water-splitting performance could be also improved by developing a method to reduce the bubble size (e.g., through the addition of surfactants) or adopting membranes that have better thermal tolerance. We hope that these results will inspire additional studies of how to increase the productivity of water electrolysis.

Supporting Information

Supporting Information is available from the Wiley Online Library or from the author.

Acknowledgements

F.Y. and M.J.K. contributed equally to this work. This work was supported in part by a National Science Foundation CAREER award (DMR-1253534), and a grant from the Duke University Energy Initiative.

Conflict of Interest

The authors declare no conflict of interest.

Keywords

flow-through electrodes, hydrogen, microfibers, porous electrodes, water splitting

Received: April 3, 2020
Revised: April 30, 2020
Published online: May 25, 2020

- [1] L. Bird, D. Lew, M. Milligan, E. M. Carlini, A. Estanqueiro, D. Flynn, E. Gomez-Lazaro, H. Holttinen, N. Menemenlis, A. Orths, P. B. Eriksen, J. C. Smith, L. Soder, P. Sorensen, A. Altiparmakis, Y. Yasuda, J. Miller, *Renew. Sustain. Energy Rev.* **2016**, 65, 577.
- [2] Twelve states produced 80% of U.S. wind power in 2013, <https://www.eia.gov/todayinenergy/detail.php?id> (accessed: September 2019).
- [3] Wind and Solar Curtailment Totals by Month, <http://www.caiso.com/informed/Pages/ManagingOversupply.aspx> (accessed: September 2019).
- [4] P. Denholm, T. Mai, *Renew. Energy* **2019**, 130, 388.
- [5] M. Götz, J. Lefebvre, F. Mörs, A. McDaniel Koch, F. Graf, S. Bajohr, R. Reimert, T. Kolb, *Renew. Energy* **2016**, 85, 1371.
- [6] A. Lewandowska-Bernat, U. Desideri, *Energy Procedia* **2017**, 105, 4569.
- [7] A. Mazza, E. Bompard, G. Chicco, *Renew. Sustain. Energy Rev.* **2018**, 92, 794.
- [8] S. Clegg, P. Mancarella, *IEEE Trans. Sustain. Energy* **2015**, 6, 1234.
- [9] P. Colbertaldo, G. Guandalini, S. Campanari, *Energy* **2018**, 154, 592.
- [10] S. Schiebahn, T. Grube, M. Robinius, V. Tietze, B. Kumar, D. Stolten, *Int. J. Hydrogen Energy* **2015**, 40, 4285.
- [11] S. Wang, B. Tarroja, L. S. Schell, B. Shaffer, S. Samuelsen, *Appl. Energy* **2019**, 235, 284.
- [12] C. van Leeuwen, M. Mulder, *Appl. Energy* **2018**, 232, 258.
- [13] M. Bailera, B. Peña, P. Lisbona, L. M. Romeo, *Appl. Energy* **2018**, 228, 1032.
- [14] A. Lewandowska-Bernat, U. Desideri, *Appl. Energy* **2018**, 228, 57.
- [15] B. Pivovar, N. Rustagi, S. Satyapal, *Electrochim. Soc. Interface* **2018**, 27, 47.
- [16] M. Reuß, T. Grube, M. Robinius, P. Preuster, P. Wasserscheid, D. Stolten, *Appl. Energy* **2017**, 200, 290.
- [17] M. E. Demir, I. Dincer, *Int. J. Hydrogen Energy* **2018**, 43, 10420.
- [18] T. Sinigaglia, F. Lewiski, M. E. Santos Martins, J. C. Mairesse Siluk, *Int. J. Hydrogen Energy* **2017**, 42, 24597.
- [19] A. Buttler, H. Spliethoff, *Renew. Sustain. Energy Rev.* **2018**, 82, 2440.
- [20] M. Carmo, D. L. Fritz, J. Mergel, D. Stolten, *Int. J. Hydrogen Energy* **2013**, 38, 4901.
- [21] B. Guinot, F. Montignac, B. Champel, D. Vannucci, *Int. J. Hydrogen Energy* **2015**, 40, 8778.
- [22] F. Grueger, F. Möhrke, M. Robinius, D. Stolten, *Appl. Energy* **2017**, 192, 551.
- [23] T. Keipi, H. Tolvanen, J. Kontinen, *Energy Convers. Manage.* **2018**, 159, 264.
- [24] J. A. Turner, *Science* **2004**, 305, 972.
- [25] F. Mueller-Langer, E. Tzimas, M. Kaltschmitt, S. Peteves, *Int. J. Hydrogen Energy* **2007**, 32, 3797.
- [26] M. Wang, Z. Wang, X. Gong, Z. Guo, *Renew. Sustain. Energy Rev.* **2014**, 29, 573.
- [27] K. C. Sandeep, S. Kamath, K. Mistry, A. Kumar M, S. K. Bhattacharya, K. Bhanja, S. Mohan, *Int. J. Hydrogen Energy* **2017**, 42, 12094.
- [28] J. Eigeldinger, H. Vogt, *Electrochim. Acta* **2000**, 45, 4449.
- [29] A. Manabe, M. Kashiwase, T. Hashimoto, T. Hayashida, A. Kato, K. Hirao, I. Shimomura, I. Nagashima, *Electrochim. Acta* **2013**, 100, 249.
- [30] J. Fischer, H. Hofmann, G. Luft, H. Wendt, *AIChE J.* **1980**, 26, 794.
- [31] S. Marini, P. Salvi, P. Nelli, R. Pesenti, M. Villa, M. Berrettoni, G. Zangari, Y. Kiros, *Electrochim. Acta* **2012**, 82, 384.
- [32] M. I. Gillespie, F. Van Der Merwe, R. J. Kriek, *J. Power Sources* **2015**, 293, 228.
- [33] M. Bodner, A. Hofer, V. Hacker, *Wiley Interdiscip. Rev.: Energy Environ.* **2015**, 4, 365.
- [34] H. Matsushima, T. Iida, Y. Fukunaka, *Electrochim. Acta* **2013**, 100, 261.
- [35] T. Iida, H. Matsushima, Y. Fukunaka, *J. Electrochem. Soc.* **2007**, 154, E112.
- [36] M.-Y. Lin, L.-W. Hourng, C.-W. Kuo, *Int. J. Hydrogen Energy* **2012**, 37, 1311.
- [37] S.-D. Li, C.-C. Wang, C.-Y. Chen, *Electrochim. Acta* **2009**, 54, 3877.
- [38] H. Matsushima, T. Nishida, Y. Konishi, Y. Fukunaka, Y. Ito, K. Kuribayashi, *Electrochim. Acta* **2003**, 48, 4119.
- [39] H. Matsushima, Y. Fukunaka, K. Kuribayashi, *Electrochim. Acta* **2006**, 51, 4190.
- [40] X. Lu, C. Zhao, *Nat. Commun.* **2015**, 6, 6616.
- [41] F. J. Pérez-Alonso, C. Adán, S. Rojas, M. A. Peña, J. L. G. Fierro, *Int. J. Hydrogen Energy* **2014**, 39, 5204.
- [42] T. N. Pham, T. Sharifi, R. Sandström, W. Siljebo, A. Shchukarev, K. Kordas, T. Wågberg, J.-P. Mikkola, *Sci. Rep.* **2017**, 7, 6112.
- [43] M. T. Y. Paul, B. B. Yee, D. R. Bruce, B. D. Gates, *ACS Appl. Mater. Interfaces* **2017**, 9, 7036.
- [44] Y.-J. Huang, C.-H. Lai, P.-W. Wu, L.-Y. Chen, *J. Electrochem. Soc.* **2010**, 157, P18.
- [45] M. A. Cruz, S. Ye, M. J. Kim, C. Reyes, F. Yang, P. F. Flowers, B. J. Wiley, *Part. Part. Syst. Character.* **2018**, 35, 1700385.
- [46] M. J. Kim, P. F. Flowers, I. E. Stewart, S. Ye, S. Baek, J. J. Kim, B. J. Wiley, *J. Am. Chem. Soc.* **2017**, 139, 277.
- [47] D. Huo, M. J. Kim, Z. Lyu, Y. Shi, B. J. Wiley, Y. Xia, *Chem. Rev.* **2019**, 119, 8972.
- [48] M. J. Kim, Y. Seo, M. A. Cruz, B. J. Wiley, *ACS Nano* **2019**, 13, 6998.
- [49] M. A. Choi, M. H. Lee, J. Chang, S. J. Lee, *J. Non-Newtonian Fluid Mech.* **1998**, 79, 585.
- [50] M. M. Tomadakis, T. J. Robertson, *J. Compos. Mater.* **2005**, 39, 163.
- [51] S. Fu, J. Song, C. Zhu, G. L. Xu, K. Amine, C. Sun, X. Li, M. H. Engelhard, D. Du, Y. Lin, *Nano Energy* **2018**, 44, 319.
- [52] Q. Zhang, N. M. Bedford, J. Pan, X. Lu, R. Amal, *Adv. Energy Mater.* **2019**, 9, 1901312.
- [53] A. J. Bard, L. R. Faulkner, *Electrochemical Methods: Fundamentals and Applications*, John Wiley & Sons, Inc., New York **2001**.
- [54] V. H. Nguyen, A. P. Sheppard, M. A. Knackstedt, W. Val Pinczewski, *J. Pet. Sci. Eng.* **2006**, 52, 54.
- [55] I. A. Beresnev, W. Deng, *Phys. Fluids* **2010**, 22, 012105.
- [56] W. Deng, M. B. Cardenas, P. C. Bennett, *Adv. Water Resour.* **2014**, 64, 34.
- [57] L. Andersson, A. Herring, S. Schlueter, D. Wildenschild, *Adv. Water Resour.* **2018**, 122, 251.
- [58] K. Singh, M. Jung, M. Brinkmann, R. Seemann, *Annu. Rev. Fluid Mech.* **2019**, 51, 429.
- [59] S. Ma, G. Mason, N. R. Morrow, *Colloids Surf. A* **1996**, 117, 273.
- [60] S. Soliman, S. Sant, J. W. Nichol, M. Khabiry, E. Traversa, A. Khademhosseini, *J. Biomed. Mater. Res., Part A* **2011**, 96A, 566.
- [61] T. G. Tranter, J. T. Gostick, A. D. Burns, W. F. Gale, *Transp. Porous Media* **2018**, 121, 597.
- [62] Z. T. Karpyn, M. Piri, *Phys. Rev. E* **2007**, 76, 016315.

- [63] P. Haug, B. Kreitz, M. Koj, T. Turek, *Int. J. Hydrogen Energy* **2017**, *42*, 15689.
- [64] J. T. Gostick, *J. Electrochem. Soc.* **2013**, *160*, F731.
- [65] M. Sabharwal, J. T. Gostick, M. Secanell, *J. Electrochem. Soc.* **2018**, *165*, F553.
- [66] A. Aghaei, M. Piri, *J. Hydrol.* **2015**, *522*, 488.
- [67] K. A. Klise, D. Moriarty, H. Yoon, Z. Karpyn, *Adv. Water Resour.* **2016**, *95*, 152.
- [68] B. Beverskog, I. Puigdomenech, *Corros. Sci.* **1997**, *39*, 969.
- [69] M. S. Burke, S. Zou, L. J. Enman, J. E. Kellon, C. A. Gabor, E. Pledger, S. W. Boettcher, *J. Phys. Chem. Lett.* **2015**, *6*, 3737.
- [70] X. Wu, B. Feng, W. Li, Y. Niu, Y. Yu, S. Lu, C. Zhong, P. Liu, Z. Tian, L. Chen, W. Hu, C. M. Li, *Nano Energy* **2019**, *62*, 117.
- [71] H. Sun, Y. Lian, C. Yang, L. Xiong, P. Qi, Q. Mu, X. Zhao, J. Guo, Z. Deng, Y. Peng, *Energy Environ. Sci.* **2018**, *11*, 2363.
- [72] Z. Qiu, C.-W. Tai, G. A. Niklasson, T. Edvinsson, *Energy Environ. Sci.* **2019**, *12*, 572.
- [73] X. Han, X. Wu, Y. Deng, J. Liu, J. Lu, C. Zhong, W. Hu, *Adv. Energy Mater.* **2018**, *8*, 1800935.
- [74] H. Zhou, F. Yu, Q. Zhu, J. Sun, F. Qin, L. Yu, J. Bao, Y. Yu, S. Chen, Z. Ren, *Energy Environ. Sci.* **2018**, *11*, 2858.
- [75] Y. Wu, X. Tao, Y. Qing, H. Xu, F. Yang, S. Luo, C. Tian, M. Liu, X. Lu, *Adv. Mater.* **2019**, *31*, 1900178.
- [76] T. Van Tam, S. G. Kang, M. H. Kim, S. G. Lee, S. H. Hur, J. S. Chung, W. M. Choi, *Adv. Energy Mater.* **2019**, *9*, 1900945.
- [77] C. Dong, T. Kou, H. Gao, Z. Peng, Z. Zhang, *Adv. Energy Mater.* **2018**, *8*, 1701347.
- [78] D. Senthil Raja, H.-W. Lin, S.-Y. Lu, *Nano Energy* **2019**, *57*, 1.
- [79] D. Senthil Raja, X. F. Chuah, S. Y. Lu, *Adv. Energy Mater.* **2018**, *8*, 1801065.
- [80] J. Y. Wang, T. Ouyang, Y. P. Deng, Y. S. Hong, Z. Q. Liu, *J. Power Sources* **2019**, *420*, 108.
- [81] X. Xu, X. Tian, Z. Zhong, L. Kang, J. Yao, *J. Power Sources* **2019**, *424*, 42.
- [82] W. Hao, R. Wu, R. Zhang, Y. Ha, Z. Chen, L. Wang, Y. Yang, X. Ma, D. Sun, F. Fang, Y. Guo, *Adv. Energy Mater.* **2018**, *8*, 1801372.
- [83] X. Yu, Z. Y. Yu, X.-L. Zhang, Y.-R. Zheng, Y. Duan, Q. Gao, R. Wu, B. Sun, M.-R. Gao, G. Wang, S.-H. Yu, *J. Am. Chem. Soc.* **2019**, *141*, 7537.
- [84] N. K. Oh, C. Kim, J. Lee, O. Kwon, Y. Choi, G. Y. Jung, H. Y. Lim, S. K. Kwak, G. Kim, H. Park, *Nat. Commun.* **2019**, *10*, 1723.
- [85] R. Phillips, A. Edwards, B. Rome, D. R. Jones, C. W. Dunnill, *Int. J. Hydrogen Energy* **2017**, *42*, 23986.
- [86] X. Yu, M. Wang, X. Gong, Z. Guo, Z. Wang, S. Jiao, *Adv. Energy Mater.* **2018**, *8*, 1802445.
- [87] M. I. Gillespie, R. J. Kriek, *J. Power Sources* **2017**, *372*, 252.
- [88] O. Schmidt, A. Gambhir, I. Staffell, A. Hawkes, J. Nelson, S. Few, *Int. J. Hydrogen Energy* **2017**, *42*, 30470.
- [89] H. Ju, S. Badwal, S. Giddey, *Appl. Energy* **2018**, *231*, 502.
- [90] M. Lehner, R. Tichler, H. Steinmüller, M. Koppe, *Power-to-Gas: Technology and Business Models*, Springer, New York **2014**.